Article

Controlling the Structural Properties and Optical Bandgap of PbO–Al₂O₃ Nanocomposites for Enhanced Photodegradation of Methylene Blue

Abdelazim M. Mebed [1,*], Alaa M. Abd-Elnaiem [2,*], Alhulw H. Alshammari [1], Taha A. Taha [1,3], Mohamed Rashad [2,4] and Dalia Hamad [2]

[1] Department of Physics, College of Science, Jouf University, Sakaka P.O. Box 2014, Saudi Arabia; ahalshammari@ju.edu.sa (A.H.A.); taha.hemida@gmail.com (T.A.T.)
[2] Physics Department, Faculty of Science, Assiut University, Assiut 71516, Egypt; m.ahmad@ut.edu.sa (M.R.); Noniatypes@yahoo.com (D.H.)
[3] Physics and Engineering Mathematics Department, Faculty of Electronic Engineering, Menoufia University, Menouf 32952, Egypt
[4] Nanotechnology Research Unit, Department of Physics, Faculty of Science, University of Tabuk, Tabuk P.O. Box 741 71491, Saudi Arabia
[*] Correspondence: amali@ju.edu.sa (A.M.M.); abd-elnaiem@aun.edu.eg (A.M.A.-E.)

Abstract: In the present work, PbO-*x* wt% Al₂O₃ nanocomposites (where *x* = 0, 10, 20, 30, 40, 50, 60, 70, and 100 wt%) were prepared by a microwave irradiation method. Their structural parameters, morphology, and chemical bonds, were investigated by X-ray diffraction (XRD), transmission electron microscopy (TEM), and Fourier-transform infrared spectroscopy (FTIR). It was noticed that the produced phases have an orthorhombic crystal structure and the smaller average crystallite sizes were formed when the ratio of Al₂O₃ is 40 wt%. The FTIR analysis reveals the formation of various bonds between Al or Pb and O. The TEM analysis reveals that the PbO-*x*%Al₂O₃ composites (*x* = 20, 40, and 60), composed of dense particles, and their size are smaller compared to the pure Al₂O₃ sample. The optical bandgap obeys the direct allowed transition and decreases from 4.83 eV to 4.35 eV as the PbO ratio in the composites increases from 0 to 100%. The intensity of the photoluminescence emission, at the same wavelength, increases as the PbO ratio increases from 0% to 60% implying that increasing the PbO content increases the capacity of free carriers within the trap centers. The prepared composites are used as a catalyst to remove the methylene blue (MB) from the wasted water under UV-visible or visible light irradiations. The photocatalytic degradation of MB was investigated by applying various kinetic models. It was found that the PbO-30% Al₂O₃, and PbO-40% Al₂O₃ composites are the best ones amongst other compositions. Furthermore, the pseudo-second-order model is the best model for describing the deterioration mechanism among the models studied. The formed composites could be suitable for the degradation of organic dyes for water purification as well as applications that required a higher optical bandgap.

Keywords: Al₂O₃; PbO; nanocomposite; hybrid; photocatalysts; structural; energy storage

1. Introduction

The pollution of the oceans, seas, and rivers is caused by numerous organic and inorganic dyes and consider a serious problem in our life [1]. The vast development of chemical and petrochemical industrial operations around the world are blamed for the spread of such dangerous compounds. There are a few examples of hazardous materials such as MB, methyl violet, methyl orange, potassium permanganate, etc. [2]. Dyes are usually poisonous due to their negative impact on environmental processes, which affects aquatic species' gills and causes spawning places and refuges to be disrupted. Therefore, continuous searching for suitable technologies since water treatment and purification

should be among the major interest in our lives. Amongst these technologies, the photocatalytic degradation of organic pollutants such as hazardous dyes is considered a promising technology for water purification [3].

The photocatalytic performance, as well as the catalytic kinetics, were extensively studied by using numerous metal oxides, complex metal oxides, sulfides, nitrides, and semiconductors-based materials such as TiO_2, ZnO, CuO, etc. [1–10]. Additionally, there are several efforts for studying the photocatalytic kinetics of various composites containing various transition metal oxides and semiconductors-based materials [1–6]. The purpose of such studies is to shift the photodegradation from the ultraviolet into the visible or/and acquire a high degradation efficiency by controlling the optical bandgap and modifying the crystal structure and morphologies of the newly formed materials [5–7]. For example, the photocatalytic performance of TiO_2 (anatase) was improved by covering with PbO clusters to form PbO/TiO_2 composite [5]. To address this issue, PbO modified TiO_2 introduced new states above the TiO_2 valence band, causing the band onset to shift into the visible. Hole localization on the PbO surface and electron localization on the TiO_2 surface is the result of this updated configuration. As a result of the PbO_2 modification of TiO_2, visible light photocatalysis occurs via new states just below the TiO_2 conduction band, resulting in hole localization on TiO_2 and electron localization on PbO_2. The structural properties of PbO/TiO_2 were affected by the change of molar ratio and hence affecting their photocatalytic efficiency towards Benzophenone-3 UV filter [6]. The doping of the prepared PbO, prepared by the hydrothermal method, with Ni enhances the photocatalytic degradation of various amounts and concentrations of methylene blue (MB) assisted by the visible light [7]. In addition, nanocomposites-based heavy metal oxide such as PbO is applied in the radiation shielding, energy storage, sensors, and ceramics industry [8,9]. Besides, metal oxide-based nanomaterials are received a huge interest from scientists and researchers due to their possible use for multifunctional applications in diverse science areas [11].

The synthesis of nanocomposites from various oxides usually reveals new properties by comparison with the individual components. For instance, Al_2O_3 exhibits a wide bandgap (~9 eV) and high dielectric constant (~9), therefore Al_2O_3 is utilized for dynamic random-access memories, organic light-emitting devices, and catalyst and absorbent applications [12]. On the other hand, the PbO and PbO_2 have good chemical stability, micro-hardness, optical transparency, and electrical conductivity which is required for the optoelectronic industry [13–15]. The production of nanocomposites with different PbO and Al_2O_3 contents could improve the physicochemical properties of the resulting $PbO-Al_2O_3$ nanocomposites. For example, the formed $PbO-Al_2O_3$ nanocomposites showed an improvement in harmful radiation shielding technology [8].

Al_2O_3 nanostructure's promising qualities qualify it for a wide range of applications in industrial and personal care goods [16–18]. Al_2O_3 nanoparticles, on the other hand, may act as free radical scavengers. These Al_2O_3 nanoparticles appear to be able to protect cells from oxidative stress-induced cell death in a way that is dependent on the particle's structure rather than its size [19]. The photocatalytic performance of MB under visible light irradiation using TiO_2 catalysts was enhanced by the formation of a TiO_2/Al_2O_3 heterostructure [20,21]. The purpose of the formation of TiO_2 heterostructure with Al_2O_3 material is due to its thermal stability and capability to deliver catalytic activity [22]. In general, Al_2O_3 has five discrete crystal phases which have denotations δ, η, γ, θ, and α-Al_2O_3. Due to the massive surface area of γ and α-Al_2O_3 for most photocatalytic reactions, they are considered as the strongest absorber [23]. There are various metal oxides are incorporated together with Al_2O_3 such as V_2O_5, Fe_2O_3, Ga_2O_3, Bi_2O_3, etc., to enhance the photocatalytic performance for removing disparate hazardous dyes [24–26]. The mechanism during electrochemical degradation of neutral red using $PbO_2/α-Al_2O_3$ composite was studied by Yao et al. [27].

The conductivity and photoluminescence (PL) properties of composite solids are increased by heterogeneous doping of insulating dispersoid in the host matrix [28]. The

increase in conductivity can be explained by several factors related to the physical and chemical properties of the composites. Among the mechanisms postulated is the space-charge layer effect [29], high concentration of point defect [30], and phase transition [31]. Porous materials, in general, can be used as composite solid electrolytes due to the enormous surface area available between the host matrix and the dispersoid [32].

In the present work, PbO-x%Al$_2$O$_3$ composites (where x = 0, 10, 20, 30, 40, 50, 60, 70, and 100 wt%) were prepared by microwave irradiation method. Their structural parameters were investigated using the XRD, FTIR, TEM, and PL techniques. Moreover, their photocatalytic performance for removing the MB from the wasted water was studied under ultraviolet-visible or visible light irradiation for various irradiation times, and different kinetics models were investigated.

2. Results and Discussion

Figure 1 shows the FTIR spectra of PbO-x%Al$_2$O$_3$ composites containing 10, 20, 30, 40, 50, 60, and 100% Al$_2$O$_3$ nanoparticles. There is an absorption peak was observed around 462 cm^{-1} related to Pb-O stretching [33], which is observed in pure PbO, whereas, in other samples, a small hump is visible [33,34]. A sharp peak was seen around 788 cm^{-1} representing the asymmetric bending vibration of Pb-O-Pb and this peak disappears in pure Al$_2$O$_3$ nanoparticles. In other words, this peak is more intense for pure PbO samples, and their intensity decreases with an increase in the percentage of Al$_2$O$_3$ nanoparticles [34,35]. There is a hump appearing between 500 and 900 cm^{-1} belonging to the vibrational frequencies of the coordinate O–Al–O bond [24,36]. The broad peak that centered around 601 cm^{-1} in the region between 500 cm^{-1} and 900 cm^{-1} is a characteristic feature of the vibrational frequencies of coordinate O–Al–O bond. The stretching vibration of the Al–O bond is also responsible for the observed peaks at 821, 722, and 569 cm^{-1} [37]. The Al–O bonds are responsible for the bands seen at 1035, 750, and 514 cm^{-1} [38]. A sharp peak was seen at 1385 cm^{-1} is a characteristic of the stretching vibration of the Al-O-Al was observed for the pure Al$_2$O$_3$. The water molecules and peaks formed in the wavenumber of 1733 cm^{-1} correspond to the flexural O-H group of the water molecule. Table 1 summarizes all of the observed FTIR peaks for more clarity and to see all of the trends and changes in the various composites.
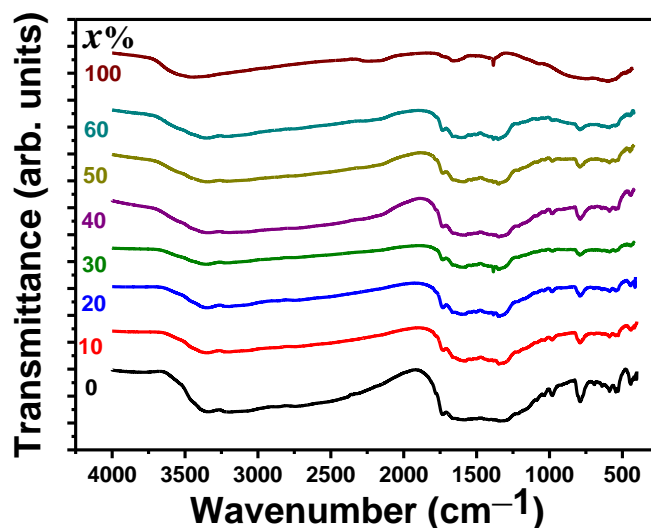

Figure 1. FTIR spectra for PbO-x%Al$_2$O$_3$ composites.

Table 1. FTIR band assignments of PdO-*x*%Al$_2$O$_3$ composites.

Wavenumber (cm^{-1})		Assignment	Ref.
In This Work	**Literature**		
~1637	1733	The H-O-H bending vibration of adsorbed water	[24,36]
1350	1385	The stretching vibration of the Al-O-Al	[38]
500–750	601	Al–O octahedral coordination givesAl–O stretching	[37]
400–500	462	Related to stretching Pb-O	[33,34]
Around 700	788	The asymmetric bending vibration of Pd-O-Pd	[33,34]

Figure 2a shows the XRD charts for the investigated PbO-*x*%Al$_2$O$_3$ composites. The pure PbO, Al$_2$O$_3$, and PbO-*x*%Al$_2$O$_3$ composites are partially crystalline with crystalline ratios close to 60%, and the rest is amorphous. In addition, the formed phases in the pure or composite samples show an orthorhombic crystal structure. There are few diffraction peaks were observed for the pure Al$_2$O$_3$ phase at 2θ = 25.58, 35.14, 37.79, 43.36, 52.55, 57.52, 66.55, and 77.23° that associated with the Miller indices of (012), (104), (110), (113), (024), (116), (214), and (119), respectively. These seen diffraction peaks were well agreed with the JCPDS No-010-0173. Also, there are few diffraction peaks were observed for the pure PbO phase at 2θ = 27.60, 30.25, and 36.25° that corresponds to the Miller indices of (120), (200), and (111), respectively. These observed diffraction peaks were well agreed with the JCPDS No-04-021-0870, which is associated with the PbO phase.
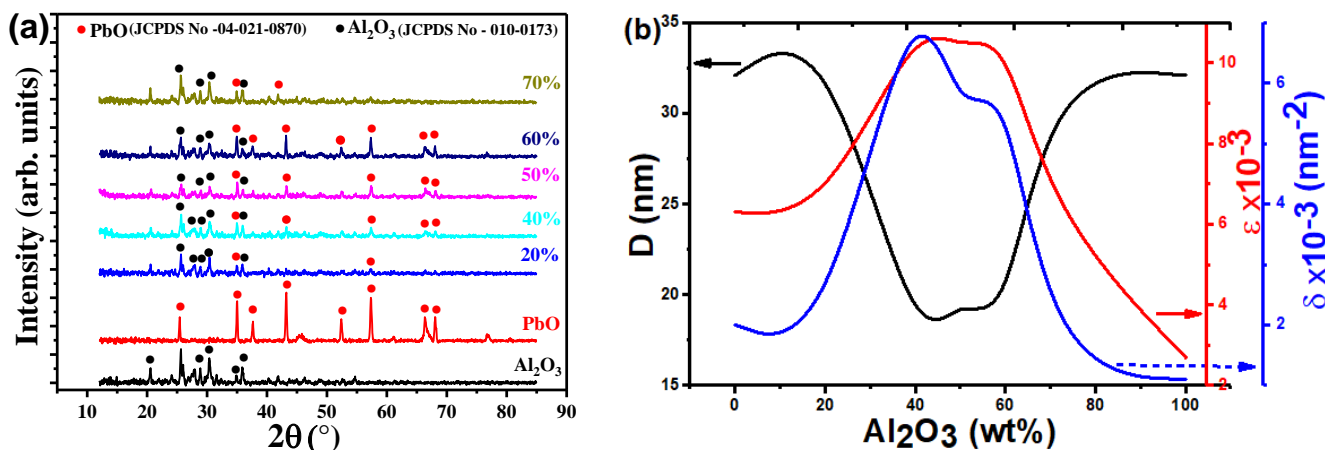
Figure 2. (**a**) XRD charts, and (**b**) average crystallite size (*D*), dislocation density (*δ*), and microstrain (*ε*) versus the percentage ratio of Al$_2$O$_3$ in PbO-*x*%Al$_2$O$_3$ composites.

The Scherrer's equation: $D = \frac{k\lambda}{\beta \cos(\theta)}$, where *k* is constant, *λ* is the wavelength, *θ* is Bragg's angle, and *β* is the full width at half maximum, was used to compute the crystallite size. In addition, the dislocation density (*δ*) and microstrain (*ε*) were determined using $\delta = \frac{1}{D^2}$, and $\varepsilon = \frac{\beta \cos(\theta)}{4}$, respectively. The average crystallite size for individual oxides, PbO and Al$_2$O$_3$, have an equivalent value which equals 32.10 nm. Meanwhile, the average crystallite for other composites is changed depending on the ratio of the oxide components. The values of the average crystallite size are 35.26, 16.45, 20.22, 17.90, and 32.71 nm for *x* equals 20, 40, 50, 60, and 70% in the PbO-*x*%Al$_2$O$_3$ composites. The smallest value for the average crystallite size was observed for PbO-40%Al$_2$O$_3$ composites. On another side, the highest value of the average crystallite size was observed for PbO-20%Al$_2$O$_3$ composites.

The investigated crystal structure parameters well agree with our previous work [8]. It was proposed in this work that the formed alloys composites formed based on the substitution of the PbO atoms by Al_2O_3 atoms as their atoms are closed together in size. The formation of such composites with smaller crystallite sizes or smaller particle sizes could be suitable for the application that required higher surface areas.

A comparison of the average crystallite size, dislocation density, and microstrain for various composites is shown in Figure 2b. It is generally observed that the average value of the structural parameters does not take specific trends with the change of Al_2O_3 ratio in the composites. The smaller value of crystallite size could be obtained in the range from 40 to 60% of Al_2O_3 concentration. As expected from the mathematical relation that provides the microstrain and dislocation density, their trend is similar but shows an opposite change to the change of the average crystallite sizes. It is widely accepted that a decrease in crystallite size, as well as a decrease in particle size, is followed by an increase in the surface area [39].

HR-TEM images at high resolving powers and a selected area electron diffraction (SAED) pattern for PbO-x% Al_2O_3 composites (x = 20, 40, 60, and 100%) are shown in Figure 3a–d, and Figure 3e–h, respectively. The HR-TEM can be used to assess the shape and size of the investigated samples in general. Particles of various shapes, such as irregularly shaped particles, have been observed. Regarding the Al_2O_3 nanoparticles (Figure 3d), the particle is dense with an average diameter of 4 nm. Meanwhile, for the PbO-x%Al_2O_3 composites with different contents of 20, 40, and 60, the dense particles are smaller compared to the pure Al_2O_3 sample. Moreover, the particles size is becoming large and reached 10 nm, which shows unclear crystalline lattices.
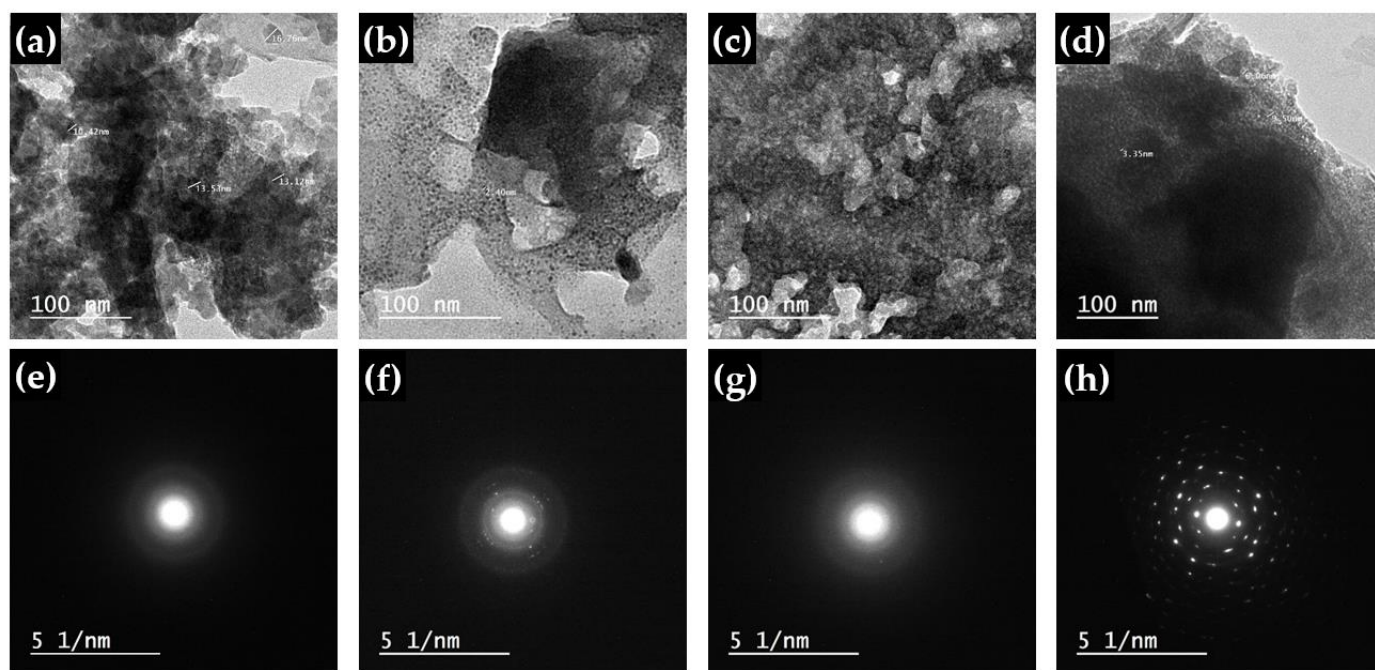

Figure 3. HR-TEM images at high resolving powers, and SAED pattern, respectively, for PbO-x%Al_2O_3 composites, where x equals (**a**,**e**) 20%, (**b**,**f**) 40%, (**c**,**g**) 60% and (**d**,**h**) 100%.

Figure 4a shows the ultraviolet-visible absorbance spectra as a function of the photon wavelength for PbO-x%Al_2O_3 composites. The curves reveal similar behavior with the wavelength as with increasing the photon wavelength the absorbance was decreased. The decrease in the absorbance value takes place suddenly for smaller wavelengths (<350 nm), while the change in the absorbance becomes smaller for higher wavelengths (>350 nm). The maximum absorbance was observed for pure Al_2O_3 samples, while the minimum value of the absorbance was seen for PbO-60%Al_2O_3 composites. The decrease in absorption at

λ < 300 nm is caused by absorption associated with point defects in the oxygen sublattice of Al_2O_3, specifically oxygen vacancies with trapped electrons [40].
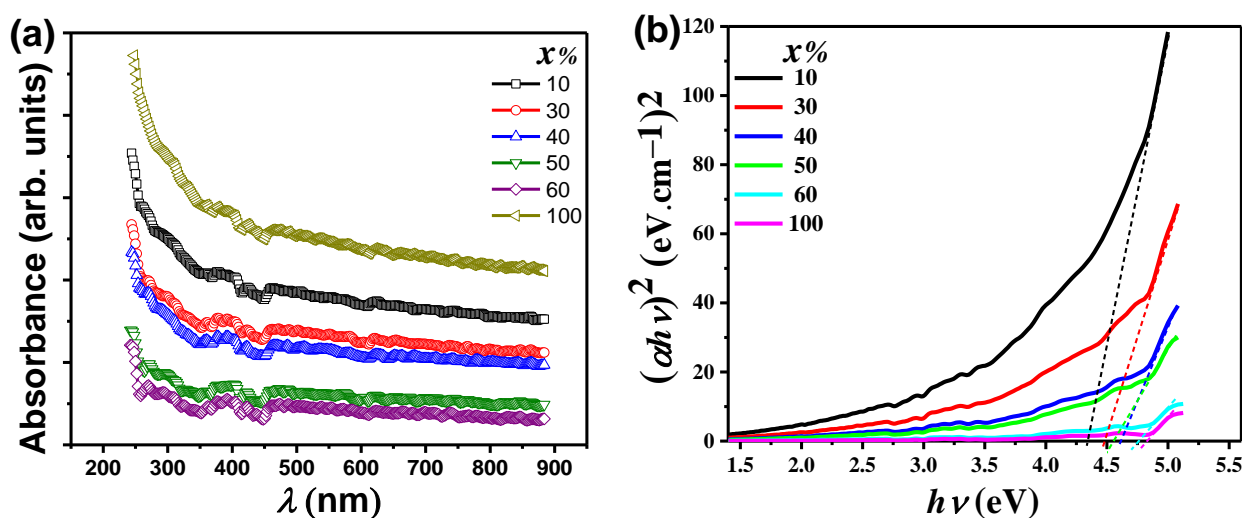

Figure 4. (**a**) UV–visible absorbance spectra versus λ, and (**b**) $(\alpha v h)^2$ versus hv for PbO-x%Al_2O_3 composites.

The UV-visible absorbance spectrum was used to calculate the energy bandgap of PbO-x% Al_2O_3 composites. Furthermore, the spectrum dependency of the absorption around the fundamental absorption edges within the framework of one electron was used to determine information about the type and mechanism of optical transitions. The experimental data of the absorbance is usually used for estimating the optical bandgap through Tauc's function [41]. Figure 4b demonstrates the relationship between $(\alpha v h)^2$ and (hv) for PbO-x%Al_2O_3 composites. These plots show the best linear fitting to the Tauc's relation $(\alpha hv)^2 = const.(hv - E_g)$, where E_g, h, and v are the optical bandgap, Plank constant, and frequency, respectively. It is noticed from the graph shown in Figure 4b that the optical transition obeys the direct allowed transition. For the extrapolation of the straight line, the optical bandgap is estimated to be equals to 4.35, 4.48, 4.61, 4.56, 4.75, and 4.83 eV for x equals 10, 30, 40, 50, 60, and 100 in PbO-x%Al_2O_3 composites, respectively. The estimated value of E_g for Al_2O_3 well agrees with other work [24]. The large values of E_g of the prepared composites which belong to the ultraviolet range allows their application to be used as good photocatalysts under the assistance of ultraviolet irradiation and can be used for other applications that require a larger optical bandgap [42] such as energy storage applications.

Figure 5 depicts the effect of PbO concentration on the PL emission bands of PbO-x% Al_2O_3 composites. According to the Tauc plot analysis (Figure 4b), the estimated optical bandgap of the PbO-x% Al_2O_3 composites is in the range of 4.35–4.83 eV. The presence of a trap center near the band edge is indicated by the PL emission from PbO-x% Al_2O_3 composites at 394 nm, which corresponds to 2.46 eV (less than the optical bandgap). Surface state defects in PbO-x% Al_2O_3 composites could be responsible for trap center formation. According to the emitted PL light, the capacity of the free carriers in the trap centers is limited for pure Al_2O_3 nanoparticles. By increasing the PbO ratio in the sample, the effect of doping with PbO nanoparticles on the PL emission of PbO-x% Al_2O_3 composites was investigated. It can be seen that the PL emission intensity at the same wavelength increases as the doping ratio increases from 0% to 60% PbO doping in PbO-x% Al_2O_3 composites. This suggests that increasing the PbO content increases the capacity of free carriers within the trap centers. As a result, more radiative paths from these trap centers are expected. The capping agent was responsible for the observed increase in PL intensity, which was followed by the expansion of nonradiative relaxation paths on the surface of PbO

nanoparticles. Increased PbO content increases PL intensity due to improved crystallinity, which is accompanied by a decrease in dangling bonds and undesirable nonradiative surface state defects. According to the preliminary results of the effect of doping in PbO-x% Al$_2$O$_3$ composites with PbO, increasing the PbO contents in the investigated composites improved the optical properties.
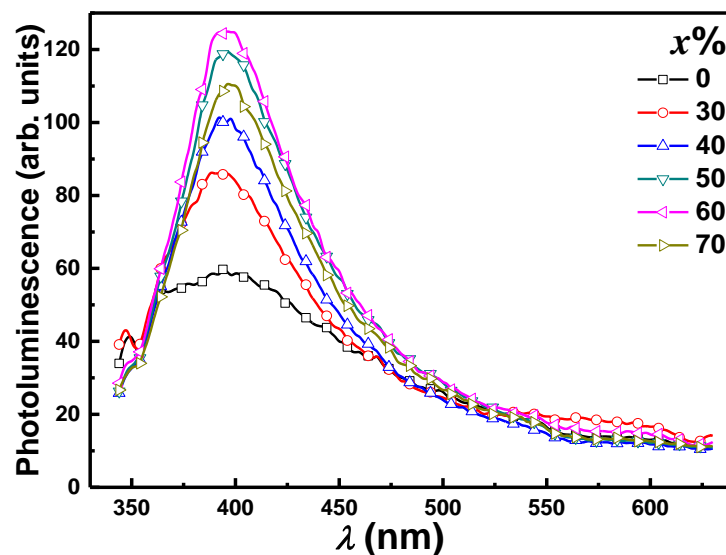

Figure 5. PL emission spectra as a function of λ for PbO-x% Al$_2$O$_3$ composites.

Apart from investigating and determining the structural and optical bandgaps of PbO-x% Al$_2$O$_3$ composites, these composites were also used as a catalyst for water purification or water decolorizations from waste dyes such as MB, with the use of ultraviolet irradiation. Figure 6a,b show the representative absorbance spectra as a function of incident radiation wavelength (λ) during the removal of MB utilizing pure PbO and Al$_2$O$_3$ nanoparticles as catalysts for different irradiation periods (up to 105 min). The occurrence of one unique maximum situated at λ = 665 nm is what characterizes the absorbance of MB solutions, according to the relationship between absorbance and λ. Furthermore, increasing the irradiation time reduces the amount of radiation absorbed by the MB solution. This decrease demonstrates the efficacy of PbO or Al$_2$O$_3$ nanoparticles as a catalyst for removing the MB dye, and hence the possibility of wastewater treatment via photocatalytic degradation processes. The absorbance was decreased from 0.90 to 0.68 for the PbO catalyst, while for the Al$_2$O$_3$ catalyst was reduced from 0.78 to 0.62 as the irradiation time reached 105 min. Similar experiments (not shown here) were carried out for the other samples that contained both PbO, and Al$_2$O$_3$ to form PbO-x%Al$_2$O$_3$ composites.

Figure 7a illustrates the MB dye photodegradation rate ($\frac{C_t}{C_o}$) versus the irradiation time (t) for PbO-x%Al$_2$O$_3$ composites. It is obvious from the figure that the PbO-40%Al$_2$O$_3$ composites showed a faster degradation rate of the MB and was reached a constant value after 20 min of the UV-visible irradiation. On another side, the PbO-10%Al$_2$O$_3$ composites revealed the highest value of photocatalytic activity compared to other composites. On the other hand, pure Al$_2$O$_3$ (100% Al$_2$O$_3$) nanoparticles had a lower photocatalytic activity value, which could be related to the greater bandgap limiting the visible absorption region. The increased photogenerated electrons and holes, which might be separated in the case of PbO nanoparticles, are the principal light absorbers for composites with a larger ratio of PbO. As a result, we may conclude that the PbO nanoparticle is a good photoelectron acceptor, trapping the photoelectron and reducing photoelectron-hole pair recombination when compared to Al$_2$O$_3$. Additional tests were performed to confirm such concerns, and the results are shown later.
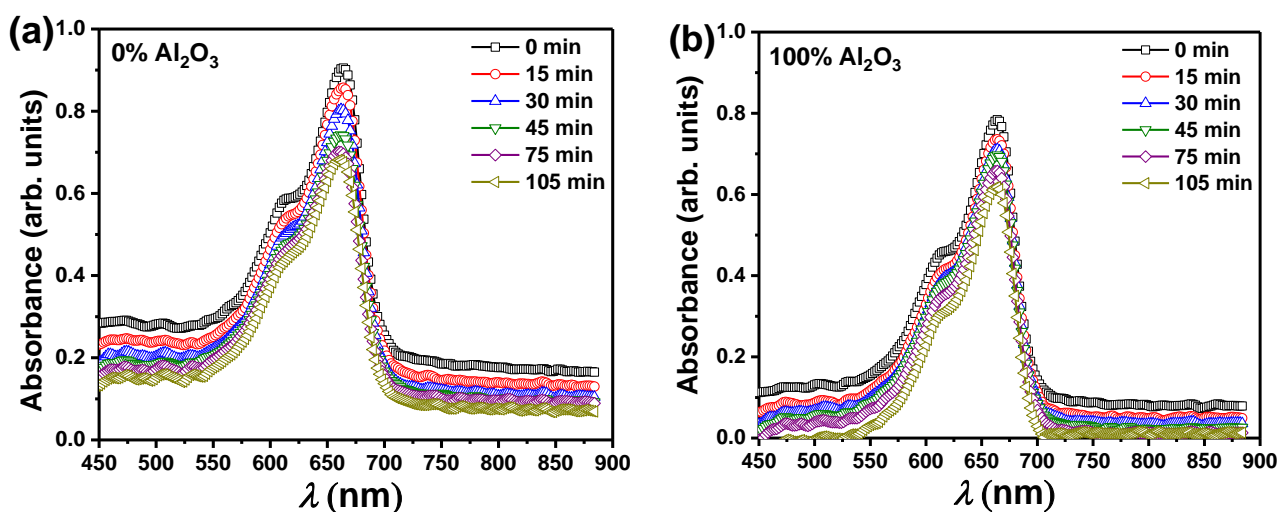
Figure 6. UV-visible absorption spectra of MB as a function of λ after photoreduction of the MB for various times using (**a**) pure PbO, and (**b**) pure Al_2O_3 nanoparticles as catalysts.
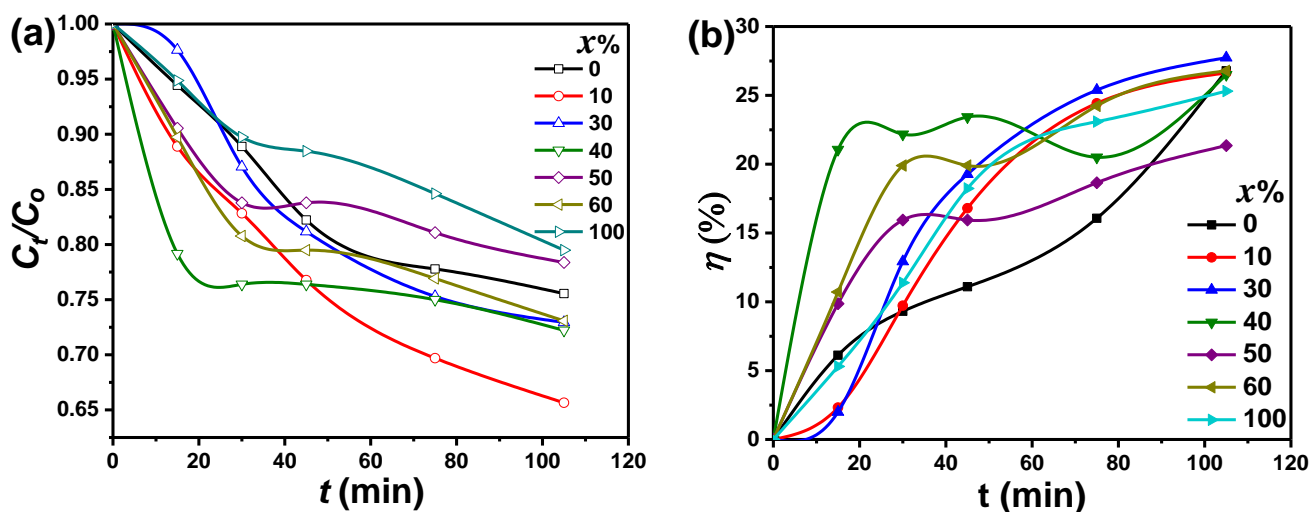

Figure 7. (**a**) The plot of concertation ratio $\left(\frac{C_t}{C_o}\right)$, and (**b**) the photocatalytic efficiency (η) at various irradiation times (*t*) of removing MB using PbO-*x*%Al_2O_3 composites as a catalyst.

　　　The following equation can be used to evaluate the removal effectiveness of MB degradation of photocatalytic (η), as well as other dyes such as potassium permanganate and methyl orange: $\eta\ (\%) = \frac{C_o - C_t}{C_o} \times 100 = \frac{A_o - A_t}{A_o} \times 100$ [24], where C_o is the waste initial concentration, C_t is the waste residual concentration after an irradiation time (*t*), A_o is the waste initial absorbance, and A_t is the waste absorbance after a fixed irradiation time. Figure 7b shows the removing efficiency of MB in the case of PbO-*x*%Al_2O_3 nanocomposites as a function of *t*. For PbO-40% Al_2O_3 nanocomposites, as shown in Figure 7b, the estimated η was significantly increased up to 23% as the irradiation time increased to 20 min, while was slightly increased up to 26% with some oscillations in the efficiency value for a further increase in the UV-visible irradiation time up to 105 min. For longer periods of UV-visible irradiation, the maximum efficiency (28%) for removing MB was observed for PbO-30%Al_2O_3 composites, while the minimum value (21%) was observed for PbO-50%Al_2O_3 composites. The PbO-30%Al_2O_3 and PbO-40%Al_2O_3 composites could be considered as the best catalysts samples, and this could be attributed to the formed smallest crystallites size according to the XRD analysis, among other parameters.

The degradation rate constants of MB dye were determined using Langmuir-Hinshelwood kinetics to further investigate the catalytic activity of PbO-x% Al$_2$O$_3$ composites. The disintegration rate of a pseudo-first-order response can be calculated using the formula: $\ln\left(\frac{C_t}{C_0}\right) = -kKt = -k_{app}t$ [43], where k is the degradation rate constant, K is the adsorption equilibrium constant, and k_{app} is the apparent rate kinetic constant or called pseudo-first-order reaction constant. The reaction rate was evaluated from $k_{app} = -\ln\left(\frac{C_t}{C_0}\right)/t$. The determined value of k_{app} for various composites was summarized in Table 2. The largest value of k_{app} is 4.6×10^{-3} min^{-1} and was observed for PbO-10%Al$_2$O$_3$ composites, while the smallest value is 2.3×10^{-3} min^{-1} and was observed for pure Al$_2$O$_3$ nanoparticles.

Table 2. Parameter values of pseudo-first-order, pseudo-second-order, and the intra-particle diffusion models, and experimental q_e for the adsorption of MB using PbO-x%Al$_2$O$_3$ composites as a catalyst.

Model	Parameters	PbO-x%Al$_2$O$_3$						
		0	10	30	40	50	60	100
Experimental q_e	q_e (exp.) (mg/g)	30.20	27.55	31.04	30.75	30.20	29.36	28.69
Pseudo-first order	K_1 (h^{-1})	0.67	2.16	0.98	1.55	1.82	2.02	1.96
	R^2	0.99	0.97	0.32	0.92	0.96	0.96	0.97
Pseudo-second order	q_e (mg/g)	33.04	32.00	34.13	33.04	33.04	33.04	32.00
	Δq_e (mg/g)	2.84	4.45	3.09	2.29	2.84	3.68	3.31
	$K_2 \times 10^{-2}$ (g/mg.min)	2.76	2.50	13.52	7.50	5.52	2.76	3.13
	R^2	1.00	1.00	1.00	1.00	1.00	1.00	1.00
Intra-particle diffusion	K_{diff} (mg/g.min$^{1/2}$)	0.23	0.42	0.20	0.19	0.25	0.31	0.30
	C (mg/g)	29.00	27.00	31.00	30.00	30.00	29.00	28.00
	R^2	0.90	0.98	0.72	0.95	0.95	0.91	0.95
Langmuir-Hinshelwood	$k_{app} \times 10^{-3}$ (min^{-1})	3.1	4.6	3.5	4.0	2.8	3.6	2.3
Elovic model	β (g.min/mg)	1.07	0.67	6.36	2.00	1.32	0.70	0.82

At any irradiation period (q_t) and equilibrium (q_e), the adsorbed masses of MB dye per unit mass of PbO-x%Al$_2$O$_3$ composites (q in mg/g) were calculated using: $q_t = (C_i - C_t)\frac{V}{W}$, and $q_e = (C_i - C_e)\frac{V}{W}$ [25]. Here, q_t is adsorbed capacity quantities of MB at a time (t), q_e is equilibrium quantities adsorbed of MB, C_i is the initial concentration of MB solution (mg/L), C_t is concentrations of adsorbate (mg/L) at the irradiation time (t), C_e is concentrations of equilibrium adsorbate (mg/L), V is the volume of MB adsorbate (L), and W adsorbent mass (g). Figure 8a shows the dependence of q_t of MB using PbO-x%Al$_2$O$_3$ composites as a catalytic at various irradiation times. The augmentation of q_t as a function of irradiation time was demonstrated, and then q_t reached saturated values. The plots that show the relation between q_t and t are quite similar to the relation η-t. The PbO-30%Al$_2$O$_3$ composite shows the highest q_t over all of the irradiation time and amongst the studied composites. The behavior of both of these relations reveals the increase of the calculated catalytic efficiency, and these values are consistent with other studies [26,27].
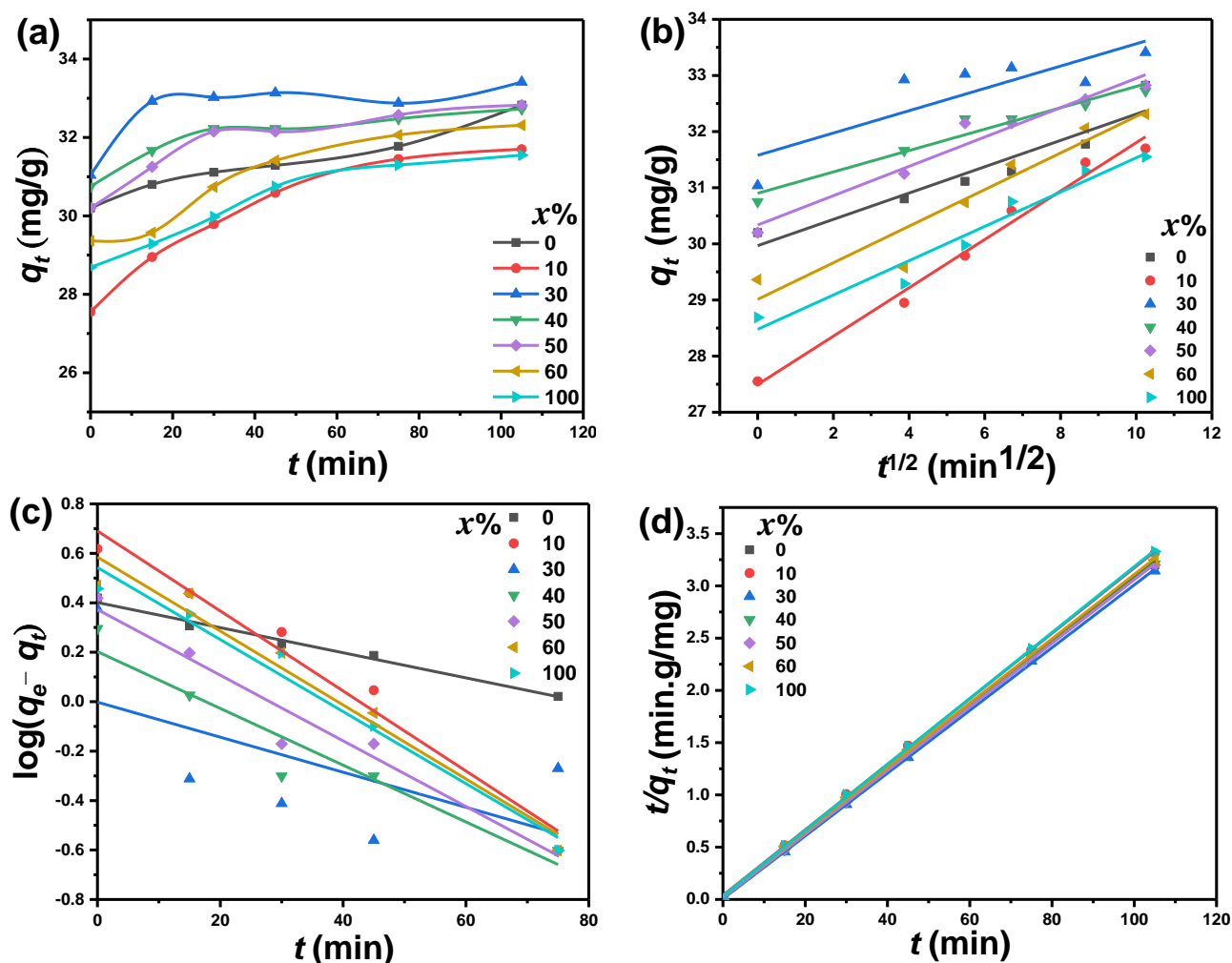
Figure 8. (**a**) Adsorption capacity (q_t) of MB, (**b**) intra-particle diffusion model, (**c**) pseudo-first-order kinetic model, and (**d**) pseudo-second-order kinetic model for the adsorption of MB using PbO-x%Al$_2$O$_3$ composites as a catalyst.

Several models are used to analyze the catalytic degradation kinetics of the obtained data. These models include the intra-particle diffusion kinetics, the pseudo-first-order, and the pseudo-second-order models. These models are represented by the following equations, respectively: $q_t = K_{diff}\sqrt{t} + C$, $\log(q_e - q_t) = \log(q_e) - \frac{K_1}{2.303}t$, and $\frac{t}{q_t} = \frac{1}{K_2 q_e^2} + \frac{t}{q_e}$ [28], where K_{diff} is intraparticle diffusion kinetic model (mg/g·min$^{1/2}$), K_1, K_2 and C are pseudo-first-order (g/mg·min), pseudo-second-order constants (g/mg·min), and kinetic parameter constants. This C value gives the boundary-layer thickness evidence. The obtained results of MB adsorption kinetic onto PbO-x%Al$_2$O$_3$ composites surface were studied using these mentioned models. The obtained data are plotted as shown in Figure 8b–d, respectively. The kinetic parameters K_{diff}, K_1, and K_2 were determined and listed in Table 2.

These values, as well as the experimental q_{max} and association coefficients (R^2), have been assessed. The dependence of q_t on $\sqrt{t}$, for MB degradation process in the case of PbO-x%Al$_2$O$_3$ composites is shown as a straight line as shown in Figure 8b. The K_{diff} and C values for PbO-x%Al$_2$O$_3$ composites were estimated by fitting these lines. The plots have a correlation coefficient (R^2) value of various from 0.75 to 0.98. Therefore, we can conclude that the intra-particle diffusion kinetic model is more suitable to describe the degradation mechanism for the adsorption of MB onto PbO-x%Al$_2$O$_3$ composites. The maximum estimated value of K_{diff} is 0.42 mg/g.min$^{1/2}$ corresponding to a lower value of C and equals 27 mg/g and was observed for PbO-10%Al$_2$O$_3$ composites. Meanwhile, the

minimum value of K_{diff}, 0.19 mg/g·min$^{1/2}$, was observed for PbO-40%Al$_2$O$_3$ composites. In general, the value of K_{diff} is changed between 0.19 and 0.42 mg/g·min$^{1/2}$, while C was changed between 27 and 31 mg/g. This designates that the adsorption of MB on PbO-x%Al$_2$O$_3$ composites has been conducted by a single step. From these results, agreement of these results with other results reported in the literature has been obtained [29].

The use of the pseudo-first-order kinetic model for MB adsorption on the presence of PbO-x% Al$_2$O$_3$ composites as a catalyst is shown in Figure 8c. Figure 8c illustrates a linear relationship between $\log(q_e - q_t)$ and t and the slope of the fitted lines were used to calculate the values of K_1. The maximum estimated values of K_1 were found to equal 2.16 h^{-1} for PbO-10%Al$_2$O$_3$ composites, while the minimum value (0.67 h^{-1}) was observed for pure PbO nanoparticles. The plotted relation between $\log(q_e - q_t)$ and t correlates values R^2 between 0.32 and 0.98. The pseudo-second-order kinetic model for MB adsorption on PbO-x%Al$_2$O$_3$ composites is shown in Figure 8d. It illustrates the plots of the relation of $\frac{t}{q_t}$ against t with a good linear fitting with R^2 equals 1 for all investigated composites. The values of K_2 are calculated from the intercepts of the fitted lines and are given in Table 2. The highest K_2 value was illustrated for PbO-30%Al$_2$O$_3$ composites and equals 13.5×10^{-2} g/mg.min, meanwhile, the minimum value was observed for PbO-10%Al$_2$O$_3$ composites and equals 2.5 g/mg.min. The average value of q_e equals 32.9 mg/g. The estimated value of q_e is in good agreement with the experimental value of q_e. In the case of the pseudo-second-order kinetic model, the correlation coefficient (R^2) is approximately one. This value is higher than the intra-particle diffusion kinetic model and the pseudo-first-order kinetic model. As a result of the correlation factor's magnitude, the pseudo-second-order kinetic model is a better fit for describing the current deterioration mechanism. The Elovic equation is another equation devised for investigating the catalytic degradation of the researched sample. In the kinetics of gas chemisorption on solids, the Elovic equation is commonly used. This Elovic equation is presented in the following equation [44]: $q_t = \frac{\ln(\alpha\beta) + \ln(t)}{\beta}$, where α is the initial sorption rate (mg/g·min), and β is a parameter in (g·min/mg). This parameter reflects the coverage of the surface as well the activation energy for chemisorption. Figure 9a illustrates the dependence of q_t on $\ln(t)$. It shows a linear behavior which hence well agrees with Elovic's kinetic model. The maximum and minimum values of β for the catalytic degradation of MB were observed in the presence of PbO-30%Al$_2$O$_3$ and PbO-60%Al$_2$O$_3$ composites and equal 6.36 g·min/mg, and 0.7 g·min/mg, respectively.
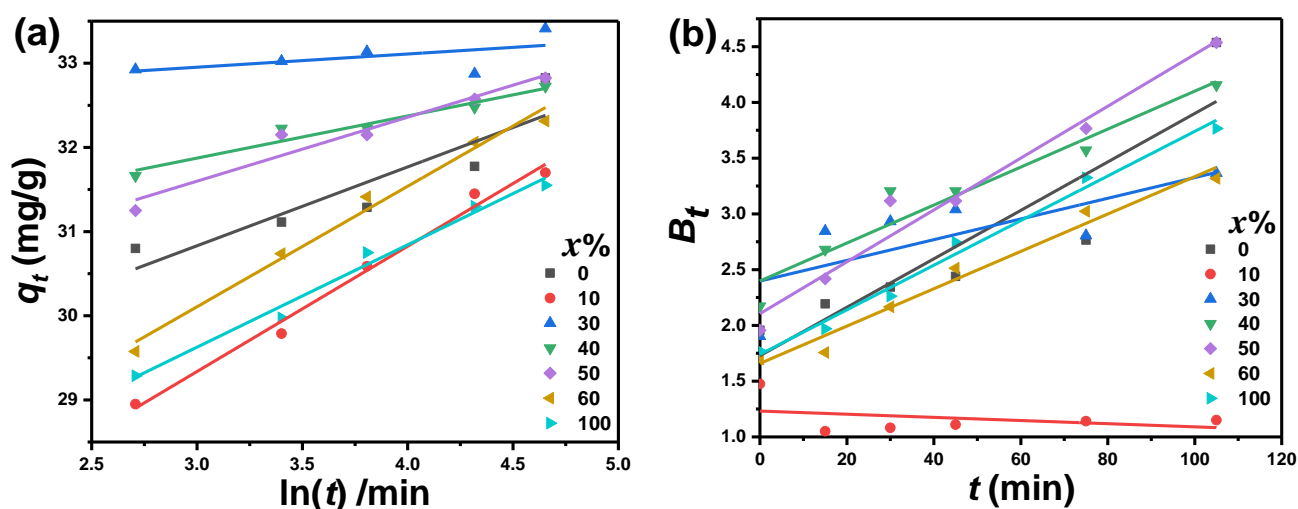

Figure 9. (**a**) the relation between the quantities adsorbed capacity (q_t) versus $\ln(t)$, and (**b**) B_t versus the irradiation time (t) for the adsorption of MB using PbO-x%Al$_2$O$_3$ composites as a catalyst.

It is well known that the adsorption process can be divided into several steps. The following are the measures to take: (i) sorption and desorption within the particle and solid's surface, (ii) diffusion on the solid's surface (film diffusion), (iii) adsorbate transport (particle diffusion), and (iv) sorption and desorption on the solid's surface [31]. Film and particle diffusions are the rate-limiting processes. Boyd et al. [45], made the suggestion a model which could be applied for investigating the diffusion mechanism during the catalytic degradation process, which mathematically written as follows [32]: $B_t = -0.4977 - \ln\left(1 - \frac{q_t}{q_e}\right)$. If the relationship between B_t versus t is linear through the origin point using this Boyd's model, the particle diffusion process is process control. If, on the other hand, this relationship predicts origin through another location, the diffusion is thought to be a rate-limiting phase. Figure 9b shows the dependence of B_t on t which shows straight lines. These lines do not intersect at the origin. As a result, the diffusion process can be thought of as a rate-limiting stage.

As is well known, oxidants increase the number of trapped electrons, preventing recombination and generating oxidizing radicals, which may enhance dye photocatalytic degradation [46]. The increase in the rate of photocatalytic degradation of MB could be attributed to an increase in MB concentration or pH [46]. As a result, changes in the dye molecule's behavior may be responsible for the change in the percentage degradation of dye at higher MB concentrations. When the substrate concentration was decreased, the degradation rate could be decreased. This could be one of the reasons why the degradation rate decreases over time. The photocatalytic activity of different photocatalysts varies due to differences in lattice mismatch, surface area, and impurities on the catalyst's surface, which affect pollutant adsorption and the lifetime and recombination rate of electron-hole pairs. A large surface area can be a deciding factor in certain photodegradation reactions, as a large amount of adsorbed organic molecules accelerates the reaction rate [47]. However, depending on particle size, the dominant mode of electron-hole recombination may differ [48]. As a result, since the PbO-40% Al_2O_3 composite has the smallest crystallite size, higher photocatalytic activity was observed.

Figure 10a depicts the absorbance spectra for the degradation of MB using PbO-40% Al_2O_3 nanocomposites as a catalyst during various periods of visible light exposure only. Figure 10b compares the photodegradation efficiency of a PbO-40% Al_2O_3 catalyst under UV-visible and visible light irradiation. In general, the absorbance decreases as the exposure time for visible light increases. When compared to UV-visible light, the photodegradation efficiency of MB using PbO-40% Al_2O_3 catalyst under visible light is acceptable. The degradation efficiency under UV-visible light is higher, particularly at low irradiation times (less than 75 min). In other words, photodegradation under UV-visible light is much faster at low irradiation times, and with the increase in the irradiation time becomes smaller and closer to photodegradation under visible light alone. For example, at the same irradiation time of 20 min, the degradation efficiency is 21% and 6%, respectively, when using PbO-40% Al_2O_3 catalyst under UV-visible light and visible light only. On the other hand, for longer irradiation times, such as 105 min, the degradation efficiency is 26.5% and 25.5%, respectively, when using PbO-40% Al_2O_3 catalyst under UV-visible light and visible light only. Such findings could demonstrate how the addition of PbO can effectively reduce the optical bandgap of the catalyst, increasing the ability to use PbO-*x*% Al_2O_3 nanocomposites as a catalyst only under visible irradiation rather than UV and visible light, particularly for longer irradiation times.
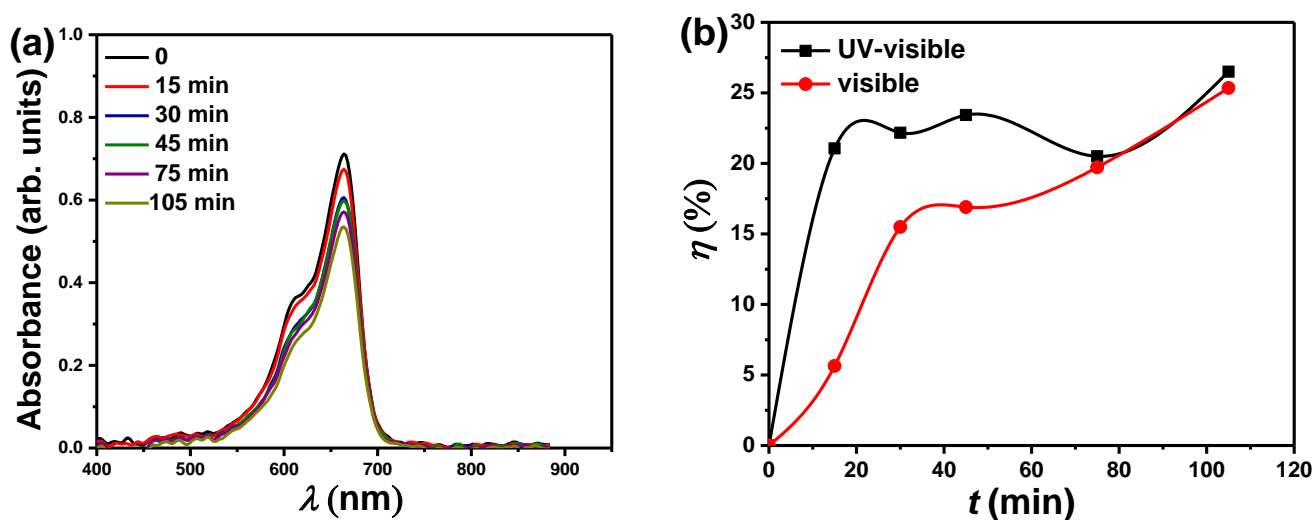
Figure 10. (**a**) The optical absorption spectrum of MB as a function of wavelength (λ) after photoreduction of the MB in the presence of PbO-40% Al_2O_3 as a catalyst for various times. (**b**) the plot compares photocatalytic efficiency (η) at different irradiation times under UV-visible light or visible light using PbO-40% Al_2O_3 as a catalyst.

3. Materials and Methods

The lead and aluminum oxides and their based composites were prepared by the microwave irradiation method and described in detail elsewhere [8]. The investigated Al_2O_3 nanoparticles were prepared by mixing 0.2 M $CO(NH_2)_2 \cdot 6H_2O$ with 0.2 M $Al(NO_3)_2 \cdot 6H_2O$ in a flask. The mixture was then placed in a microwave oven with a 650 W power setting for 20 min. The final formed powder of the Al_2O_3 nanoparticle has a white color. Similar procedures were applied to produce a PbO_2 nanoparticle from $Pb(NO_3)_3 \cdot 9H_2O$ as a precursor material. The two combinations of these metal oxides (M_1-O & M_2-O) could be blended by mechanical mixing with chemical connections of M_1-O-M_2 as available previously for nanocomposites made of Al_2O_3 and PbO_2 [8,43]. The XRD was used to check the formation of pure oxides of Al_2O_3 and PbO_2, however it was revealed that the formed oxides are Al_2O_3 and PbO (instead of PbO_2). These findings will be confirmed later. The unit of all mentioned percentage ratios of oxides in composites proposed in this study is weight percentage.

The chemical bonding of the generated PbO-x% Al_2O_3 composites was investigated using an FTIR, model Termo-Nicolet-6700 FT-IR. The FTIR spectra of various PbO-x% Al_2O_3 composites were acquired at wavenumbers ranging from 400 to 4000 cm^{-1}. The XRD technique, model Bruker D8 advanced diffractometer, Germany, was used to examine the crystal structure and other structural parameters of the composites. The XRD tool is connected to a Cu sealed tube X-ray source, which emits Cu-k_α radiation with a wavelength of 15.46 nm. The JCPDS-ICDD helped analyze the XRD charts and define the crystal structure. The XRD was acquired at a diffraction angle (2θ) between 10 and 85 °C. The structural properties of PbO-x% Al_2O_3 nanocomposites were examined using high-resolution transmission electron microscopy (HR-TEM), model JEOL, JEM 2100, Japan. In addition, for light and dark-field TEM at 200 kV, scanning image analysis was used. The PL spectra of all PbO-x% Al_2O_3 nanocomposites were measured at room temperature using a JASCO FP-6300 spectrofluorometer at an excitation wavelength of 325 nm.

An ultraviolet-visible-near-IR double-beam spectrophotometer (Perkin Elmer 750 Lamda) was used to detect absorption. The optical absorbance measurements were taken at room temperature and wavelengths ranging from 200 to 900 nm. The photocatalytic performance was tested for MB as an organic waste in the presence of PbO-x%Al_2O_3 composites. In 10 mL of 10^{-5} M of MB, 20 mg of each PbO-x% Al_2O_3 sample was added. To guarantee that the catalyst was dispersed throughout the MB solution, the solution was placed in

an ultrasonic device for 10 min. Next, the mixture of MB and catalyst was transferred to glass tubes for the irradiation process. The mixture-containing tubes were subjected to an ultraviolet light source (with a power of 285 W) and were separated by 15 cm from the UV source. For samples that were UV irradiated for 15, 30, 45, 75, and 105 min, the absorbance of the MB solution in the presence of PbO-x% Al_2O_3 composites as catalysts were assessed.

4. Conclusions

Different compositions of PbO-x%Al_2O_3 composites (where x = 0, 10, 20, 30, 40, 50, 60, 70 and 100 wt%) were synthesized using the microwave irradiation method. The structural parameters and optical bandgap, E_g, and their photocatalytic degradation of methylene blue were investigated using various models. The samples are partly crystalline and have an orthorhombic crystal structure. The crystallite size, microstrain, and dislocation density are significantly influenced by the concentration of the composite components, for example, the smaller average crystallite sizes were formed when the ratio of Al_2O_3 is 40 wt%. The FTIR analysis confirms the formation of various chemical bonds such as Al-O and Pb-O. The TEM analysis shows that the PbO-x%Al_2O_3 composites with x = 20, 40, and 60, consist of dense particles, and their size is smaller compared to the pure Al_2O_3. The optical bandgap was affected by the composition of the composites as it varies from 4.35 eV to 4.83 eV and it obeys the direct allowed transition. The intensity of the PL emission at the same wavelength increases with increasing PbO content up to 60% in PbO-x% Al_2O_3 composites, emphasizing that increasing the PbO content increases the capacity of free carriers within the trap centers. Accordingly, under UV-visible or visible light irradiation, the prepared composites exhibited good catalytic performance in removing MB from wastewater, particularly for composites with a higher PbO ratio and for longer irradiation times. Among the investigated models, the pseudo-second-order model is the best at describing the deterioration mechanism. The prepared PbO-x%Al_2O_3 composites could qualify for the degradation of some organic dyes for water purification assisted by UV irradiation and could be used for other applications that required a high optical bandgap as that for energy storage.

Author Contributions: Conceptualization, A.M.M., A.M.A.-E., and M.R.; methodology, M.R., T.A.T. and D.H.; validation, A.M.M., A.M.A.-E.; M.R., and D.H.; formal analysis, A.M.M.; investigation, A.M.A.-E.; resources, D.H. and T.A.T.; data curation, A.H.A.; writing—original draft preparation, A.M.M., A.M.A.-E.; M.R., and D.H.; writing—review and editing, A.M.M. and A.M.A.-E.; Visualization, M.R. and T.A.T.; supervision, M.R.; project administration, A.M.M.; funding acquisition, A.M.M. All authors have read and agreed to the published version of the manuscript.

Data Availability Statement: Data are available on demand.

Conflicts of Interest: The authors declare no conflict of interest.

References

1. Gouvea, C.A.K.; Wypych, F.; Moraes, S.G.; Durán, N.; Nagata, N.; Peralta-Zamora, P. Semiconductor-assisted photocatalytic degradation of reactive dyes in aqueous solution. *Chemosphere* **2000**, *40*, 433–440. [CrossRef]
2. Abd-Elnaiem, A.M.; El-Baki, R.F.A.; Alsaaq, F.; Orzechowska, S.; Hamad, D. Composite Nanoarchitectonics of Graphene Oxide for Better Understanding on Structural Effects on Photocatalytic Performance for Methylene Blue Dye. *J. Inorg. Organomet. Polym. Mater.* **2021**. [CrossRef]
3. Abd-Elnaiem, A.M.; Abdel-Rahim, M.A.; Abdel-Latief, A.Y.; Mohamed, A.A.-R.; Mojsilović, K.; Stępniowski, W.J. Fabrication, Characterization and Photocatalytic Activity of Copper Oxide Nanowires Formed by Anodization of Copper Foams. *Materials* **2021**, *14*, 5030. [CrossRef] [PubMed]

4. Porotnikova, N.M.; Eremin, V.A.; Farlenkov, A.S.; Kurumchin, E.K.; Sherstobitova, E.A.; Kochubey, D.I.; Ananyev, M.V. Effect of AO Segregation on Catalytical Activity of La0.7A0.3MnO$_3 \pm \delta$ (A = Ca, Sr, Ba) Regarding Oxygen Reduction Reaction. *Catal. Lett.* **2018**, *148*, 2839–2847. [CrossRef]

5. Bhachu, D.S.; Sathasivam, S.; Carmalt, C.J.; Parkin, I.P. PbO-modified TiO$_2$ thin films: A route to visible light photocatalysts. *Langmuir* **2014**, *30*, 624–630. [CrossRef] [PubMed]

6. Wang, Z.; Deb, A.; Srivastava, V.; Iftekhar, S.; Ambat, I.; Sillanpää, M. Investigation of textural properties and photocatalytic activity of PbO/TiO$_2$ and Sb$_2$O$_3$/TiO$_2$ towards the photocatalytic degradation Benzophenone-3 UV filter. *Sep. Purif. Technol.* **2019**, *228*, 115763. [CrossRef]

7. Borhade, A.V.; Tope, D.R.; Uphade, B.K. An efficient photocatalytic degradation of methyl blue dye by using synthesised PbO nanoparticles. *E-J. Chem.* **2012**, *9*, 705–715. [CrossRef]

8. Ali, A.M.; Issa, S.A.M.; Ahmed, M.R.; Saddeek, Y.B.; Zaid, M.H.M.; Sayed, M.; Somaily, H.H.; Tekin, H.O.; Sidek, H.A.A.; Matori, K.A.; et al. Promising applicable heterometallic Al$_2$O$_3$/PbO$_2$ nanoparticles in shielding properties. *J. Mater. Res. Technol.* **2020**, *9*, 13956–13962. [CrossRef]

9. Bratovcic, A. Synthesis, characterization, applications, and toxicity of lead oxide nanoparticles. In *Lead Chemistry*; IntechOpen Limited 5 Princes Gate Court: London, UK, 2020.

10. Rashad, M.; Shaalan, N.M.; Abd-Elnaiem, A.M. Degradation enhancement of methylene blue on ZnO nanocombs synthesized by thermal evaporation technique. *Desalination Water Treat.* **2016**, *57*, 26267–26273. [CrossRef]

11. Per-Olof, L.; Andersson, A. Complete oxidation of CO, ethanol, and ethyl acetate over copper oxide supported on titania and ceria modified titania. *J. Catal.* **1998**, *179*, 72–89.

12. Rodríguez, J.A.; Fernández-García, M. *Synthesis, Properties and Applications of Oxide Nanoparticles*; Whiley: New Jersey, NJ, USA, 2007.

13. Najafi, E.; Amini, M.M.; Behmagham, F.; Shaabani, N.; Shojaei, N. Crystal structure and luminescence properties of a new nanostructure lead (II) complex: A precursor for preparation of pure phase nanosized PbO. *Chem. Rev. Lett.* **2019**, *2*, 13–20.

14. Simon, M.; Ford, R.A.; Franklin, A.R.; Grabowski, S.P.; Menser, B.; Much, G.; Nascetti, A.; Overdick, M.; Powell, M.J.; Wiechert, D.U. Analysis of lead oxide (PbO) layers for direct conversion X-ray detection. *IEEE Symp. Conf. Rec. Nucl. Sci.* **2004**, *7*, 2035–2040.

15. Li, J.; Guo, M.; Shao, Y.; Yu, H.; Ni, K. Electrocatalytic Properties of a Novel β-PbO$_2$/Halloysite Nanotube Composite Electrode. *ACS Omega* **2021**, *6*, 5436–5444. [CrossRef]

16. Prashanth, P.A.; Raveendra, R.S.; Krishna, R.H.; Ananda, S.; Bhagya, N.P.; Nagabhushana, B.M.; Lingaraju, K.; Naika, H.R. Synthesis, characterizations, antibacterial and photoluminescence studies of solution combustion-derived α-Al$_2$O$_3$ nanoparticles. *J. Asian Ceram. Soc.* **2015**, *3*, 345–351. [CrossRef]

17. Sadiq, I.M.; Chowdhury, B.; Chandrasekaran, N.; Mukherjee, A. Antimicrobial sensitity of Escherichia coli to alumina nanoparticles. *Nanomed. Nanotechnol. Biol. Med.* **2009**, *5*, 282–286. [CrossRef] [PubMed]

18. Ruparelia, J.P.; Chatterjee, A.K.; Duttagupta, S.P.; Mukherji, S. Strain specificity in antimicrobial activity of silver and copper nanoparticles. *Acta Biomater.* **2008**, *4*, 707–716. [CrossRef]

19. Mohammad, G.; Mishra, V.K.; Pandey, H.S. Antioxidant properties of some nanoparticle may enhance wound healing in T2DM patient. *Dig. J. Nanomater. Biostructures* **2008**, *3*, 159–162.

20. Tan, L.; Dong, W.; Liu, K.; Luo, T.; Gu, X. Thermal decomposition in-situ preparation of gray rutile TiO$_2$-x/Al$_2$O$_3$ composite and its enhanced visible-light-driven photocatalytic properties. *Opt. Mater.* **2021**, *111*, 110716. [CrossRef]

21. Logar, M.; Kocjan, A.; Dakskobler, A. Photocatalytic activity of nanostructured γ-Al$_2$O$_3$/TiO$_2$ composite powder formed via a polyelectrolyte-multilayer-assisted sol-gel reaction. *Mater. Res. Bull.* **2012**, *47*, 12–17. [CrossRef]

22. Boissière, C.; Nicole, L.; Gervais, C.; Babonneau, F.; Antonietti, M.; Antonietti, H.; Sanchez, C.; Grosso, D. Nanocrystalline mesoporous γ-alumina powders "UPMC1 Material" gathers thermal and chemical stability with high surface area. *Chem. Mater.* **2006**, *18*, 5238–5243. [CrossRef]

23. Farahmandjou, M.; Golabiyan, N. Synthesis and characterization of Alumina (Al$_2$O$_3$) nanoparticles prepared by simple sol-gel method. *Int. J. Bio-Inorg. Hybr. Nanomater.* **2016**, *5*, 73–77.

24. Hakimi, M.; Morvaridi, M.; Hosseini, H.A.; Alimard, P. Preparation, characterization, and photocatalytic activity of Bi$_2$O$_3$-Al$_2$O$_3$ nanocomposite. *Polyhedron* **2019**, *170*, 523–529. [CrossRef]

25. Bekakria, H.; Bendjeffal, H.; Djebli, A.; Mamine, H.; Metidji, T.; Benrdjem, Z. Heterogeneous sono-photo-Fenton degradation of methyl violet 10B using Fe$_2$O$_3$-Al$_2$O$_3$-Ga$_2$O$_3$ as a new photocatalyst. *Inorg. Nano-Met. Chem.* **2021**, *51*, 1759–1774. [CrossRef]

26. Fu, X.; Tang, W.; Ji, L.; Chen, S. V$_2$O$_5$/Al$_2$O$_3$ composite photocatalyst: Preparation, characterization, and the role of Al$_2$O$_3$. *Chem. Eng. J.* **2012**, *180*, 170–177. [CrossRef]

27. Yao, Y.; Teng, G.; Yang, Y.; Ren, B.; Cui, L. Electrochemical degradation of neutral red on PbO$_2$/α-Al$_2$O$_3$ composite electrodes: Electrode characterization, byproducts and degradation mechanism. *Sep. Purif. Technol.* **2019**, *227*, 115684. [CrossRef]

28. Patro, L.N.; Hariharan, K. Fast fluoride ion conducting materials in solid state ionics: An overview. *Solid State Ion.* **2013**, *239*, 41–49. [CrossRef]

29. Hao, J.; Li, Y.; Liao, R.; Liu, G.; Liao, Q.; Chao, T. Fabrication of Al$_2$O$_3$ nano-structure functional film on a cellulose insulation polymer surface and its space charge suppression effect. *Polymers* **2017**, *9*, 502. [CrossRef]

30. Lagerlöf, K.P.D.; Grimes, R.W. The defect chemistry of sapphire (α-Al$_2$O$_3$). *Acta Mater.* **1998**, *46*, 5689–5700. [CrossRef]

31. Cava, S.; Tebcherani, S.M.; Souza, I.A.; Pianaro, S.A.; Paskocimas, C.A.; Longo, E.; Varela, J.A. Structural characterization of phase transition of Al_2O_3 nanopowders obtained by polymeric precursor method. *Mater. Chem. Phys.* **2007**, *103*, 394–399. [CrossRef]

32. Ngai, K.S.; Subramaniam, R.T.; Kasi, R.; Juan, J.C. A review of polymer electrolytes: Fundamental, approaches and applications. *Ionics* **2016**, *22*, 1259–1279. [CrossRef]

33. Arulmozhi, K.T.; Mythili, N. Studies on the chemical synthesis and characterization of lead oxide nanoparticles with different organic capping agents. *AIP Adv.* **2013**, *3*, 122122. [CrossRef]

34. Timar, V.; Lucăcel-Ciceo, R.; Ardelean, I. Structural studies of iron doped $3B_2O_3 \cdot 0.7PbO \cdot 0.3Ag_2O$ glasses by FT-IR and Raman spectroscopies. *Semicond. Phys. Quantum Electron. Optoelectron.* **2008**, *11*, 221–225. [CrossRef]

35. Lee, D.H.; Condrate, R.A. FTIR spectral characterization of thin film coatings of oleic acid on glasses: I. Coatings on glasses from ethyl alcohol. *J. Mater. Sci.* **1999**, *34*, 139–146. [CrossRef]

36. Shah, J.; Ranjan, M.; Gupta, S.K.; Sonvane, Y. Surfactant-assisted morphological studies of α-Al2O3 nanoparticles. In *AIP Conference Proceedings*; AIP Publishing LLC: Melville, NY, USA, 2018; Volume 1961.

37. Hemalatha, J.; Prabhakaran, T.; Nalini, R.P. A comparative study on particle–fluid interactions in micro and nanofluids of aluminium oxide. *Microfluid. Nanofluidics* **2011**, *10*, 263–270. [CrossRef]

38. Vazquez, A.; López, T.; Gómez, R.; Bokhimi; Morales, A.; Novaro, O. X-ray diffraction, FTIR, and NMR characterization of sol–gel alumina doped with lanthanum and cerium. *J. Solid State Chem.* **1997**, *128*, 161–168. [CrossRef]

39. Bueno-Ferrer, C.; Parres-Esclapez, S.; Lozano-Castell, D.; Bueno-López, A. Relationship between surface area and crystal size of pure and doped cerium oxides. *J. Rare Earths* **2010**, *28*, 647–653. [CrossRef]

40. Popov, A.I.; Lushchik, A.; Shablonin, E.; Vasil'chenko, E.; Kotomin, E.A.; Moskina, A.M.; Kuzovkov, V.N. Comparison of the F-type center thermal annealing in heavy-ion and neutron irradiated Al_2O_3 single crystals. *Nucl. Instrum. Methods Phys. Res. Sect. B Beam Interact. Mater. At.* **2018**, *433*, 93–97. [CrossRef]

41. Tauc, J.; Grigorovici, R.; Vancu, A. Optical properties and electronic structure of amorphous germanium. *Phys. Status Solidi* **1966**, *15*, 627–637. [CrossRef]

42. Zhang, Z.; Lai, Y.; Zhang, Z.; Zhang, K.; Li, J. Al_2O_3-coated porous separator for enhanced electrochemical performance of lithium sulfur batteries. *Electrochim. Acta* **2014**, *129*, 55–61. [CrossRef]

43. Rashad, M.; Hamdalla, T.A.; Garni, S.E.A.; Darwish, A.A.A.; Seleimf, S.M. Optical and electrical behaviors in NiO/xFe_2O_3 nanoparticles synthesized by microwave irradiation method. *Opt. Mater.* **2018**, *75*, 869–874. [CrossRef]

44. Cheung, C.W.; Porter, J.F.; McKay, G. Elovich equation and modified second-order equation for sorption of cadmium ions onto bone char. *J. Chem. Technol. Biotechnol.* **2000**, *75*, 963–970. [CrossRef]

45. Boyd, G.E.; Adamson, A.W.; Myers, L.S., Jr. The exchange adsorption of ions from aqueous solutions by organic zeolites. II. Kinetics1. *J. Am. Chem. Soc.* **1947**, *69*, 2836–2848. [CrossRef]

46. Reza, K.M.; Kurny, A.S.W.; Gulshan, F. Parameters affecting the photocatalytic degradation of dyes using TiO_2: A review. *Appl. Water Sci.* **2017**, *7*, 1569–1578. [CrossRef]

47. Watson, S.S.; Beydoun, D.; Scott, J.A.; Amal, R. The effect of preparation method on the photoactivity of crystalline titanium dioxide particles. *Chem. Eng. J.* **2003**, *95*, 213–220. [CrossRef]

48. Zhang, Z.; Wang, C.C.; Zakaria, R.; Ying, J.Y. Role of particle size in nanocrystalline TiO_2-based photocatalysts. *J. Phys. Chem. B* **1998**, *102*, 10871–10878. [CrossRef]